PHOTONICS Research

Gate voltage control of helicity-dependent photocurrent and polarization detection in $(Bi_{1-x}Sb_x)_2Te_3$ topological insulator thin films

Shenzhong Chen,[1] Jinling Yu,[1,5] Xiyu Hong,[2] Kejing Zhu,[2] Yonghai Chen,[3,4] Shuying Cheng,[1] Yunfeng Lai,[1] Ke He,[2,6] and Qikun Xue[2]

[1]Institute of Micro/Nano Devices and Solar Cells, School of Physics and Information Engineering, Fuzhou University, Fuzhou 350108, China
[2]State Key Laboratory of Low-Dimensional Quantum Physics, Department of Physics, Tsinghua University, Beijing 100084, China
[3]Key Laboratory of Semiconductor Materials Science, Institute of Semiconductors, Chinese Academy of Sciences, Beijing 100083, China
[4]College of Materials Science and Opto-Electronic Technology, University of Chinese Academy of Sciences, Beijing 100049, China
[5]e-mail: jlyu@semi.ac.cn
[6]e-mail: kehe@mail.tsinghua.edu.cn

Received 11 May 2023; revised 5 September 2023; accepted 14 September 2023; posted 18 September 2023 (Doc. ID 494932); published 26 October 2023

Optical helicity provides us with an effective means to control the helicity-dependent photocurrent in the spin-momentum-locked surface states of topological insulators (TIs). Also, the TIs show potential in polarization detection as an intrinsic solid-state optical chirality detector for easier integration and fabrication. However, the complex photoresponses with the circular photogalvanic effect, the linear photogalvanic effect, and the photon drag effect in the TIs prevent them from direct chirality detection of the elliptically polarized light. Here, by fitting with the theoretical models to the measured photocurrents, the microscopic origin of different components of the helicity-dependent photocurrent has been demonstrated. We show a comprehensive study of the helicity-dependent photocurrent in $(Bi_{1-x}Sb_x)_2Te_3$ thin films of different thicknesses as a function of the light incident angle and the gate-tuned chemical potential. The observation of the light incident angle dependence of the helicity-dependent photocurrent provides us with a polarization detection strategy using a TI thin film without the use of any additional optical elements, and the detection accuracy can be enhanced by gate tuning. Additionally, the Stokes parameters can be extracted by arithmetic operation of photocurrents measured with different incident angles and gating voltages for complete characterization of the polarization states of a light beam. Using this means, we realize the polarization detection and the Stokes parameters analysis with a single device. Our work provides an alternative solution to develop miniaturized intrinsic polarization-sensitive photodetectors.

https://doi.org/10.1364/PRJ.494932

1. INTRODUCTION

Polarization is more than a physical property of light, which can carry and distinguish information. The state of polarization characterizing electric field oscillation is important in imaging, display, and information storage [1–4]. For example, when light interacts with materials such as organic molecules with chiral structures the change of the polarization state can reflect their chemical and physical information like the structure symmetry, chemical composition, and other properties [1]. Thus, optical chirality detection is essential for modern optoelectronic applications, such as biomedical sensing, quantum communications and computing, liquid crystal displays, astronomy, and telecommunications [2,3,5,6]. The conventional polarization detection solutions normally require a combination of phase retarders, polarizers, quarter-wave plates, and rotating optomechanical components [4,7,8]. This is because the common semiconductors used to make photodetectors lack an intrinsic chiral response, which increases the difficulties and cost in the miniaturization and integration of devices. Using intrinsically chiral materials as a substitute can be one direction to avoid the installation of bulky and rigid optical elements. Halide perovskites have been found to be one of the promising polarization materials that meet the need for low cost, flexibility, tunable polarization sensitivity, and superior optoelectronic properties [9–15]. More recently, metamaterials demonstrate the capability to manipulate polarization states as well, which has been applied to fabricate ultracompact optical elements for direct chirality detection [16–20]. Nevertheless, a photodetector made by intrinsically chiral materials or metamaterials requires too much of a fabrication effort.

Topological insulators (TIs) may be one of the favorable materials for intrinsic solid-state polarization detection devices

with easier integration. Much attention in condensed-matter physics has been recently directed toward understanding the electronic properties of spin-polarized carriers in 3D topological insulators. The 3D TIs have metallic surface states showing linear dispersion over the insulating bulk states. In these systems, the resulting spin-polarized carriers have spins locked perpendicular to their linear momentum due to the time-reversal invariant protecting them from backscattering of any nonmagnetic impurity [21–31]. Hence, the carriers in the surface states with one spin orientation flow in a particular direction. The spin-momentum locking in the topological surface states offers a unique opportunity for spintronic, optic, and optoelectronic applications [32–36]. Until now, optical methods have been adopted as one of the main approaches to control the spin-polarized currents in 3D TIs [37–41]. In particular, circularly polarized light can induce a directional helicity-dependent photocurrent in 3D TIs, which is one of the most notable manifestations of the electronic chirality of surface states [42,43]. However, these polarization-dependent photocurrents can be generated by the circular photogalvanic effect (CPGE), the linear photogalvanic effect (LPGE), and the photon drag effect [36,42,44–48], which prevent it from direct chirality detection of the elliptical polarized light. If one can differentiate these photocurrents to obtain the CPGE and LPGE currents separately under the polarization detection, it will make the 3D TIs promising in chirality detection or Stokes parameter analysis [49].

In this paper, we report a strategy for linear and circular polarization detection using a topological insulator $(Bi_{1-x}Sb_x)_2Te_3$ thin film, which does not require complex microfabrication and additional optical elements. We first performed a comprehensive experimental study of the photocurrent response for polarized light incident on the 3D TI $(Bi_{1-x}Sb_x)_2Te_3$ thin films and found that the photoresponses of the circularly and linearly polarized light are both dependent on the incident angle of the light. Further studies of the incident angle dependence of the photocurrents allowed us to extract the different components of the polarization-dependent photocurrents, including the CPGE, LPGE, circular photon drag effect (CPDE), and linear photon drag effect (LPDE). On this basis, we realized the circular polarization detection by comparing the measured photocurrents to the calibrated results under two measurements at opposite incident angles. In addition, the accuracy of circular polarization detection can be enhanced by back gating. What is more, the linear polarization of the light can also be detected when applying proper back gating; hence, the Stokes parameters can be obtained by measuring the photocurrent on different detection modes. To the best of our knowledge, the method we have proposed to realize intrinsic optical chirality detection by a single device is new, and offers a promising platform based on topological insulators for optoelectronic applications and photodetection technologies.

2. EXPERIMENTAL DETAILS

The samples used in the experiment to investigate the helicity-dependent photocurrents and the polarization detection are ternary topological insulator $(Bi_{1-x}Sb_x)_2Te_3$ thin films named BST. The $(Bi_{0.9}Sb_{0.1})_2Te_3$ thin films with thicknesses of 10- and 20-quintuple layers (QL) and the 7-QL $(Bi_{0.8}Sb_{0.2})_2Te_3$ thin films are grown on insulating $SrTiO_3$ (STO) substrates with molecular beam epitaxy. The BST films are manually cut into Hall-bar shapes with indium contacts deposited on the surface of the BST films. The 2D electron densities determined by Hall measurements are $n = 0.56 \times 10^{13}$ cm^{-2}, 3.17×10^{13} cm^{-2}, and 3.94×10^{13} cm^{-2} for the 7-, 10-, and 20-QL samples at 77 K, respectively. The samples are mounted on an optical cryostat with a 1 Pa low-pressure chamber after bonding in the air. This cryostat also allows for the variation of the temperature in the range of 77–300 K.

A diode-pumped solid-state continuous wave laser with a wavelength of 1064 nm was adopted as the radiation source. The laser passed through a chopper (229 Hz), a polarizer, and a quarter-wave plate, and then illuminated the center of the sample, as shown in Fig. 1(a). The photocurrent was first amplified/filtered by a current preamplifier and then measured by a lock-in amplifier at the chopping frequency. After passing a lens with a focus of 20 cm, the light spot with a diameter of about 0.8 mm was focused on the sample. An optical attenuator was adopted to change the light power illuminated on the sample.

To investigate the dependence of the photocurrent in BST on incident angles, we changed the incident angle θ from −40° to +40° with the laser beam incident in the x–z plane and the photocurrent measured along the y direction, as shown in Fig. 1(a). To extract the polarization-dependent photocurrent from the total photocurrent, we fit the polarization state dependent photocurrent to [26,41,47]

$$J_{\text{total}} = C \sin 2\varphi + L_1 \sin 4\varphi + L_2 \cos 4\varphi + D, \quad (1)$$

where φ is the angle between the initial plane of polarization and the optical axis of the quarter-wave plate. The coefficient C of sin 2φ represents the helicity-dependent photocurrent induced by CPGE or CPDE. The L_1 and L_2 terms indicate the photoresponses due to linearly polarized light, which may originate from the LPGE or LPDE. The D term is the polarization-independent current, which arises from the photovoltaic effect or the Dember effect [42,50,51].

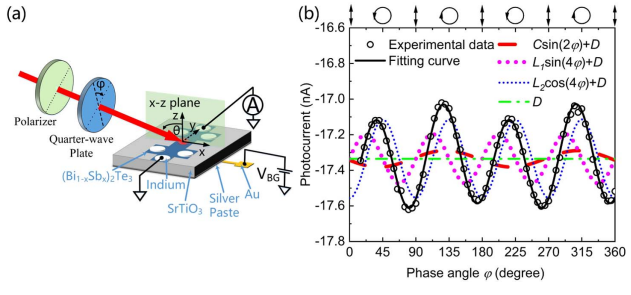

Fig. 1. (a) Schematic diagram of the device structure and measurement geometry. (b) Photocurrent as a function of the phase angle φ of the 10-QL $(Bi_{0.9}Sb_{0.1})_2Te_3$ sample when the light spot is illuminated at oblique incidence of $\theta = 30°$. The solid line (black) is the fitting curve using Eq. (1). The dotted lines (purple and blue) and the dashed line (red) are the photocurrent induced by linearly and circularly polarized light, respectively. The dash-dotted line (green) indicates the polarization-independent current D.

Besides, the measurements of the back gate tuning of the polarization-dependent photocurrent in 3D TIs are performed by applying a direct current gate voltage to the drain contact and the back gate of the insulating $SrTiO_3$ substrate. All measurements under back gating are carried out at a temperature of 77 K. For the ionic liquid gating modulated CPGE measurement, the ionic liquid (DEME-TFSI) is dropped on the surface of the sample and then covered by a quartz coverslip.

3. RESULTS AND DISCUSSION

A. Polarization-Dependent Photocurrents Analysis

To use the electronic chirality of the topological surface states for polarization detection, let us first investigate the light incident angle dependence of the photocurrent in 3D TI BST thin films. This is because the dependence of the photocurrent on the incident angle may provide an important parameter that can be adopted to detect the polarization state of light.

At a certain incident angle, the measured photocurrent can be well fitted by Eq. (1) to extract each term of the polarization-dependent photocurrents, and the typical fitting result is shown in Fig. 1(b). By fitting, we can determine the helicity-dependent photocurrent C, and the photocurrent induced by linearly polarized light, i.e., L_1 and L_2, of the 7-, 10-, and 20-QL BST samples at different incident angles, as shown in Fig. 2.

Figure 2(a) shows the helicity-dependent photocurrent (HDPC), which includes CPGE and CPDE, as a function of incident angle θ in the 7-, 10- and 20-QL BST samples under an ungated condition. The results are obtained by fitting Eq. (1) to polarization-dependent photocurrents measured at different light incident angles. Note that the HDPC in BST varies as an odd function of θ. This should be attributed to the generation mechanism of the CPGE and CPDE with the inversion asymmetry of the topological surface states. The CPGE current arises from the asymmetric excitation of states in k space due to the transfer of the angular momentum from photons to free carriers, ignoring the linear momentum transfer of photons [26,41,42,50]. However, the CPDE current is due to the transfer of both linear and angular momenta from the photons to the free carriers [44,52]. Besides, the CPGE and CPDE are both restricted by crystal symmetry [41,42,44,52]. The bulk states of 3D TIs belong to D_{3d} symmetry, and they will not generate CPGE and CPDE due to inversion symmetry [41]. For the surface states with a reduced symmetry of C_{3v}, the CPGE current that flows perpendicular to the incident plane is proportional to sin θ, while that from CPDE is proportional to sin 2θ [41], which can be expressed by [41,50,53]

$$J_y^{\mathrm{CPGE}} = \frac{A_{\mathrm{CPGE}} \sin\theta\cos^2\theta}{n_\omega\left(\cos\theta + \sqrt{n_\omega^2 - \sin^2\theta}\right)\left(n_\omega^2\cos^2\theta + \sqrt{n_\omega^2 - \sin^2\theta}\right)}, \tag{2a}$$

$$J_y^{\mathrm{CPDE}} = \frac{A_{\mathrm{CPDE}} \sin 2\theta\cos^2\theta}{n_\omega\left(\cos\theta + \sqrt{n_\omega^2 - \sin^2\theta}\right)\left(n_\omega^2\cos^2\theta + \sqrt{n_\omega^2 - \sin^2\theta}\right)}. \tag{2b}$$

Here, θ is the incident angle, and n_ω is the refractive index of the BST films, which is adopted to be 6 [26]. A_{CPGE} and A_{CPDE} are the coefficients proportional to the spin-orbit coupling (SOC) strength of the sample. The fitting curve using $J_y^C = J_y^{\mathrm{CPGE}} + J_y^{\mathrm{CPDE}}$ is shown by a solid line in Fig. 2(a). Note that the experimental data can be well fitted by the theoretical phenomenological formula, and by fitting, we obtain $J_y^{\mathrm{CPGE}}/J_y^{\mathrm{CPDE}}$, which is about 6.34, 4.62, and 2.11 for the 7-, 10- and 20-QL samples, respectively. This indicates the dominance of CPGE over CPDE in all these samples. Therefore, we mainly focus on CPGE in the following discussion. At a certain incident angle, the HDPC of the 7-QL sample shows an opposite sign to that of the 10- and 20-QL samples. This is because the HDPC is dominated by the bottom surface states, while that of the 10- and 20-QL samples are dominated by the top surface states, which is confirmed by the CPGE measurement under the front and back illuminations (see the discussion below).

Then we move to find the origin of the linear polarization-dependent components L_1 and L_2, since they are important for polarization detection. Figures 2(b) and 2(c) show the dependence of the L_1 and L_2 components on the incident angle, respectively. The solid symbols indicate the experimental data.

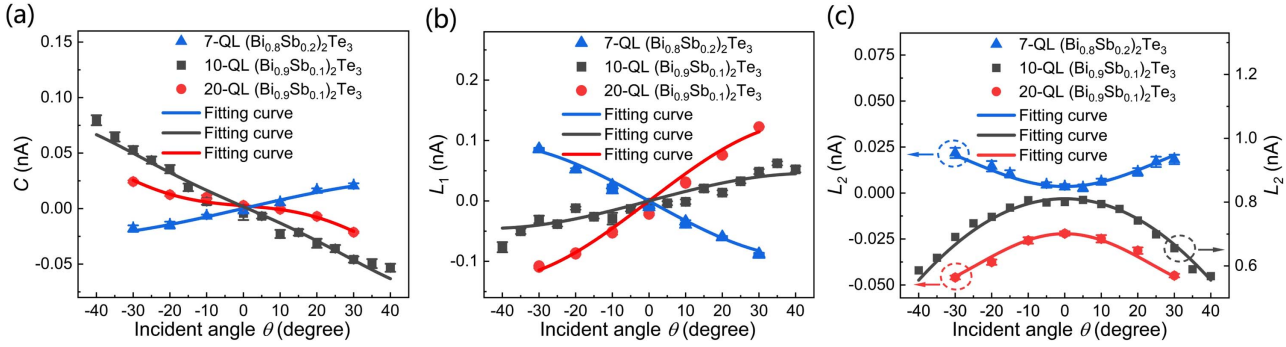

Fig. 2. Dependence of the coefficients (a) C, (b) L_1, and (c) L_2 on the light incident angle (θ), which are extracted by fitting Eq. (1) to the polarization-dependent photocurrent of the 7-QL $(Bi_{0.8}Sb_{0.2})_2Te_3$, 10-QL $(Bi_{0.9}Sb_{0.1})_2Te_3$, and 20-QL $(Bi_{0.9}Sb_{0.1})_2Te_3$ samples. The solid curve in (a) is the fitting curve by using $J_y^{\mathrm{CPGE}} + J_y^{\mathrm{CPDE}}$ expressed by Eq. (2). The solid curves in (b) and (c) represent the fitting curve by using Eq. (7) and Eq. (8), respectively.

Note that the L_1 term shows an odd function of θ while the L_2 term varies as an even function of θ for all the samples.

The linear polarization-dependent photocurrent can be attributed to LPGE or LPDE. Now let us separate these two photocurrents, since the separation of LPGE and LPDE will be helpful in polarization detection. To generate LPGE, the system should have inversion symmetry breaking. Therefore, the surface states with C_{3v} symmetry in BST will generate LPGE, while the bulk states, which belong to D_{3d} symmetry, will not generate LPGE. The LPGE current can be described by the phenomenological equation [45]

$$J_y^{\mathrm{LPGE}} = -\chi E_0^2 t_p t_s \sin\theta_0 \sin 4\varphi + \chi'(t_0 E_0)^2 \cos\theta_0 \cos 4\varphi. \tag{3}$$

Here, χ and χ' are the linearly independent components of the third-rank tensor at oblique incidence and normal incidence, respectively. E_0 is the electric field amplitude of the light wave. $t_0 = 2/(n_\omega + 1)$ is the amplitude of the transmission coefficient for normal incidence, and n_ω is the refractive index of the BST films. θ_0 is the refraction angle related to θ by $\sin\theta_0 = \sin\theta/n_\omega$. t_s and t_p are the amplitudes of the Fresnel transmission coefficients for the s- and p-polarized lights, respectively. This equation reveals that the LPGE will contribute to both L_1 and L_2 terms.

The LPDE has a different origin compared to the LPGE because it results from a dynamical alignment of carrier momenta without the requirement for inversion asymmetry [36]. The LPDE can be generated in the bulk states as well as in the surface states. With the LPDE considered, the L_2 component induced by linearly polarized light flowing along y direction can be expressed as [36]

$$J_y^{L_2} = -\frac{E_0}{2} \cos 4\varphi[(\chi' - T_z q \cos\theta)(t_s^2 + t_p^2\cos^2\theta) + T_\parallel q t_p^2 \sin^2\theta \cos\theta]. \tag{4}$$

Here, T_z, $T_\parallel$, and χ' are the coefficients representing the photon drag effect at normal incidence, the photon drag effect at oblique incidence, and the photogalvanic effect at normal incidence, respectively. q is the magnitude of the photon wave vector. However, if we fit Eq. (4) to the incident angle dependent L_2 terms, we can only obtain the fitting value of $\chi' - T_z q \cos\theta$ and $T_\parallel$, and we cannot separate each component of T_z and χ'. To differentiate the LPGE and LPDE contributions, we should further analyze the microscopic theory of the photon drag effect [36]. In 3D TIs system, it has been found that T_z will be substantially smaller than $T_\parallel$ at the high radiation frequency of incident light, since they have different frequency dependences. The relation between T_z and $T_\parallel$ can be expressed as [36]

$$\frac{T_z}{T_\parallel} \sim \frac{1 + (\omega\tau_{\mathrm{tr}})^2}{(\omega\tau_{\mathrm{tr}})^2} \frac{\varepsilon_F}{m_0 v_0^2}, \tag{5}$$

where $\omega = 2\pi f$ is the angular frequency of the radiation electric field of the light, τ_{tr} is the transport relaxation time, ε_F is the energy of Fermi level, m_0 is the mass of the electron, and v_0 is the Dirac Fermion velocity. Equation (5) demonstrates that, because the radiation magnetic field affects elastic scattering weaker than the electric field, T_z is substantially smaller than $T_\parallel$ [36]. This is because $m_0 v_0^2 \sim 10$ eV, resulting in the factor $\varepsilon_F/m_0 v_0^2$ to be on the order of 10^{-1} to 10^{-2} for BST samples [36].

Therefore, the contribution from T_z to the LPDE can be neglected at a high radiation frequency of incident light for $\lambda = 1064$ nm. Thus, Eq. (4) can be reduced to

$$J_y^{L_2} = -\frac{E_0}{2} \cos 4\varphi[\chi'(t_s^2 + t_p^2\cos^2\theta) + T_\parallel q t_p^2 \sin^2\theta \cos\theta]. \tag{6}$$

By fitting Eq. (6) to the incident angle dependence of the L_2 term, we find that the fitting value of χ' is significantly smaller than that of $T_\parallel$, which suggests that the LPGE contribution at normal incidence (χ') can be neglected. Based on the discussion above, L_1 and L_2 components can be phenomenologically expressed as

$$L_1 = \gamma \sin\theta \sin 4\varphi, \tag{7}$$

$$L_2 = \tau \sin^2\theta \cos\theta \cos 4\varphi. \tag{8}$$

Here, $\gamma = -\chi E_0^2 t_p t_s$ and $\tau = -\frac{E_0}{2} T_\parallel q t_p^2$, which are related to the LPGE and LPDE, respectively. The solid lines in Figs. 2(b) and 2(c) show that these two functions fit well, confirming that the L_1 term is contributed by the LPGE and the L_2 term mainly comes from the LPDE. In addition, the L_1 and L_2 terms of the 7-QL sample show opposite signs to that of the 10- and 20-QL samples. This should be attributed to the fact that the photocurrent of the 7-QL sample is mainly dominated by the bottom surface, while those of the 10- and 20-QL samples are mainly contributed by the top surface, which is confirmed by the analysis in the following discussion.

B. Gate Tuning of the Polarization-Dependent Photocurrents

Electrostatic gating is one of the best methods to manipulate the helicity-dependent photocurrent of the topological surface states by tuning its chemical potential. We find it is also a potent tool to tune the photodetection performance of 3D TIs. Now we discuss the deep tuning of different polarization-dependent photocurrents by electrical gating.

The dependence of the CPGE and LPGE on back gate voltages, which are shown in Fig. 3, is obtained by fitting Eq. (1) to the polarization-dependent photocurrent. Figure 3(a) shows that the CPGE currents of both the 10- and 20-QL $(Bi_{0.9}Sb_{0.1})_2Te_3$ samples are linearly tuned by the back gate voltage. Meanwhile, the sheet resistances of the 10- and 20-QL samples are linearly tuned by the back gate voltage, as shown in Fig. 4(a), and their monotonic decrease reveals that the carrier type of the two $(Bi_{0.9}Sb_{0.1})_2Te_3$ samples is n-type [51,54]. This linear dependence indicates that the Fermi level is always above the Dirac point at all the back gate voltages we adopted. The negative gating brings down the Fermi level of the surface states, suppressing the scattering between the surface-Dirac electrons and the bulk state electrons, and the positive gating raises the Fermi level into the conduction band, enhancing this kind of scattering [47,51]. As a result, the CPGE current of the two $(Bi_{0.9}Sb_{0.1})_2Te_3$ samples changes linearly with the back gating.

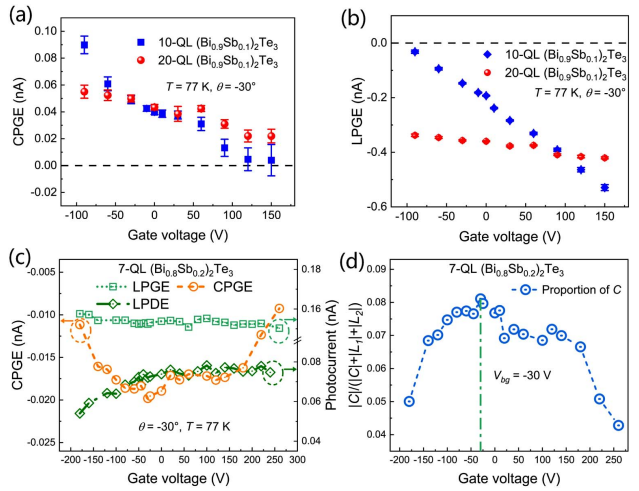

Fig. 3. Dependence of (a) CPGE and (b) LPGE currents of the 10- and 20-QL BST samples on the gate voltage, measured under $\theta = -30°$ at 77 K. (c) Dependence of the CPGE, LPGE, and LPDE currents on the gate voltage for the 7-QL BST sample measured at the incident angle $\theta = -30°$ at 77 K. (d) Dependence of the value of $|C|/(|C| + |L_1| + |L_2|)$ on the gate voltage, which is the ratio of $|C|$ to the sum of the absolute values of the polarization-dependent photocurrents $(|C| + |L_1| + |L_2|)$.

Figure 3(c) shows that the CPGE current of the 7-QL $(Bi_{0.8}Sb_{0.2})_2Te_3$ sample reaches its peak value at $V_{bg} \approx -30$ V. Besides, the value of $|C|/(|C| + |L_1| + |L_2|)$, which is the ratio of $|C|$ to the sum of the absolute values of the polarization dependent photocurrents, and the sheet resistance of the 7-QL sample also achieve their maximum values at $V_{bg} \approx -30$ V, as shown in Fig. 3(d) and Fig. 4(b), respectively. This phenomenon suggests that the Fermi level of this 7-QL sample is tuned across the Dirac point under the back gating [54]. At a back gate voltage of −30 V, the Fermi level is located at the Dirac point, in which the scattering between the surface-Dirac electrons and the bulk state electrons is minimum, leading to the maximum CPGE current. As the back gate voltage deviates from −30 V, the Fermi level will move toward the bulk bands, as shown in the inset of Fig. 4(b). Then, the scattering between the surface-Dirac electrons and the bulk state electrons increases, leading to a drop in the CPGE current [49].

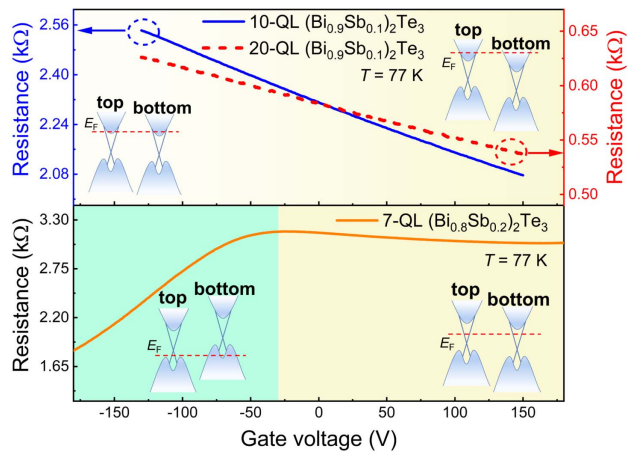

Fig. 4. Dependence of the sheet resistance on the gate voltage for (a) the 10- and 20-QL $(Bi_{0.9}Sb_{0.1})_2Te_3$ samples and (b) the 7-QL $(Bi_{0.8}Sb_{0.2})_2Te_3$ sample at 77 K. The inset shows the schematic drawing of the position of Fermi level for the BST samples under different back gate voltages.

Moreover, it can be seen from Fig. 3(a) that the CPGE current in the 20-QL BST sample is more effectively tuned by the back gate voltage, which may indicate that the CPGE current mainly comes from the top surface states. This is because the back gating will more effectively tune the Fermi level of the bottom surface states than that of the top surface states. As a result, the tuning effect of the top surface states will be less significant in the thicker sample compared to the thinner one.

To confirm our speculation, we measured the CPGE currents under the front and back illuminations. Figure 5(a) shows the experimental geometry, and Figs. 5(b), 5(c), and 5(d) show the CPGE current under the front and back illuminations of 1064 nm light for the 10-, 20-, and 7-QL samples, respectively. The experiment is carried out at room temperature. Since the top surface states show an opposite spin helicity to that of the bottom surface states, their CPGE current will also present opposite signs [55,56].

In Fig. 5(b), the CPGE current of the 10-QL sample under front illumination shows an opposite sign to that under the back illumination. This phenomenon indicates that the top surface states play the dominant role under the front illumination while the bottom surface states dominate the CPGE under the back illumination, which can be explained by the phenomenological analysis. Specifically speaking, the CPGE for the

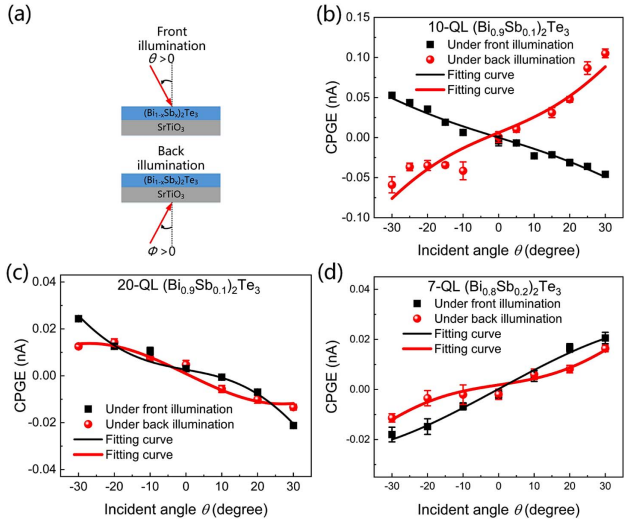

Fig. 5. Light incident angle dependence of the CPGE current under the front and back illuminations at room temperature for the 10- and 20-QL $(Bi_{0.9}Sb_{0.1})_2Te_3$ samples. (a) Schematic illustrations of the CPGE measurement under the front and back illuminations. (b)–(d) Dependence of the CPGE current on the incident angle under the front and back illuminations for the 10-QL $(Bi_{0.9}Sb_{0.1})_2Te_3$ sample, the 20-QL $(Bi_{0.9}Sb_{0.1})_2Te_3$ sample, and the 7-QL $(Bi_{0.8}Sb_{0.2})_2Te_3$ sample. The solid lines are the fitting curves using Eq. (2a).

surface states of BST with C_{3v} symmetry can be expressed by $J_y^{\mathrm{CPGE}} = \gamma_{yx}\hat{e}_x E_0^2 P_{\mathrm{circ}}$. Here, J_y^{CPGE} is the CPGE current flowing along the y direction, γ_{yx} is the second-rank pseudo-tensor for C_{3v} point group, and $\hat{e}_x$ is the unit vector pointing in the direction of the light propagation [50]. Under the front and back illumination geometries, the $\hat{e}_x$ remains the same for a certain incident angle. Therefore, if the sign of the CPGE current reverses under opposite illuminations, the dominant contribution of the CPGE must switch from the top surface states to the bottom surface states, or vice versa. Since the light intensity that reaches the top surface is stronger under the front illumination than that under the back illumination, it can be inferred that CPGE in the 10-QL BST is dominated by the top surface states under front illumination. Because the CPGE current of the 20-QL sample shows the same sign as that of the 10-QL sample under the same incident angle, while that of the 7-QL sample shows an opposite sign, the CPGE current of the 20- and 7-QL samples should be mainly contributed by the top and the bottom surface states, respectively, in the case of front illumination. The results of CPGE currents under the front and back illuminations confirm that the CPGE of both the 10- and 20-QL samples is dominated by the top surface states, which is consistent with the observation of the back gate tuning of the CPGE current in the 10- and 20-QL samples.

In addition to the CPGE current being successfully tuned by the back gate voltage, the LPGE current can also be modulated by back gating, as shown in Fig. 3(b). The back gating dependence of the LPGE currents illustrates that the LPGE of BST can be effectively tuned by the gating voltage. It can be seen that the amplitude of the LPGE increases with an increase in the back gate voltage. This is because as the back gate voltage increases, the Fermi level moves upward, leading to the increase of the carrier density and stronger scattering of carriers [49,57]. Since LPGE is due to the asymmetry scattering of free carriers on phonons, static defects, or other carriers in non-centrosymmetric media [50], the stronger scattering of carriers will increase the LPGE. The unchanged sign of the LPGE current of the 10- and 20-QL samples under back gating agrees with the gate voltage dependence of their resistance. The fact that the CPGE and LPGE currents of the thinner film are more tunable confirms that the CPGE and LPGE in the 10- and 20-QL samples are mainly contributed by the top surface states, since it is more difficult to tune the Fermi level of the top surface states in the thicker films by back gating. This result is consistent with that observed in the CPGE measurements under the front and back illuminations.

Furthermore, we also tune the CPGE current of the BST by the ionic liquid top gate. Ionic liquid gating has higher carrier density tunability than conventional top gating [41]. This is because the ionic liquid has a very high dielectric constant and, when forming an electric double-layer transistor, an extremely high electric field can be achieved within the ionic liquid. Besides, the ionic liquid is transparent, and thus can be used for photoelectric experiments [58].

The dependence of the CPGE current of the 20-QL sample on ionic liquid gating voltages is shown in Fig. 6(c), with the experimental setup illustrated in Fig. 6(a). The gating voltage is applied between the Au gate electrode and the indium electrode

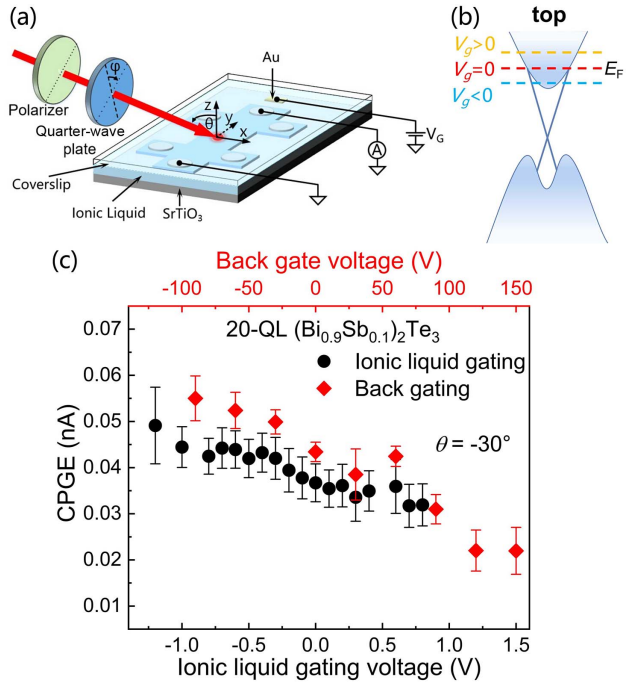

Fig. 6. (a) Schematic diagram of the device structure and measurement geometry for the modulation of the CPGE by ionic liquid gating. (b) Schematic drawing of the band structure and the Fermi level position of the BST thin film under different ionic liquid voltages. (c) Comparison of the gating voltage dependence of the CPGE current under the back and top gatings for the 20-QL BST sample measured at $\theta = -30°$.

on the 20-QL BST film. When applying a positive gating voltage, the Fermi level moves upward, as shown in Fig. 6(b). This will lead to larger scattering between the surface-Dirac electrons and the bulk state electrons. As a result, the CPGE current decreases. Similarly, the negative gating voltage will move down to the Fermi level and reduce the scattering, which will increase the CPGE current. Figure 6(c) shows that the dependence of the CPGE current on the top ionic liquid gating has the same trend as that under the back gating. This phenomenon further confirms that the CPGE of BST is mainly contributed by the top surface states, since the top gating mainly tunes the top surface states. It can be also seen from Fig. 6(c) that the CPGE can be more effectively tuned by top ionic liquid gating compared to the back gating, because obtaining the same tuning effect requires smaller gating voltages under ionic liquid gating.

C. Polarization and Stokes Parameters Detection

The complete polarization state can be described by a set of independent Stokes parameters including the total intensity S_0, two linear components S_1 and S_2, and the chiral component S_3. In addition to Stokes parameters, a fully polarized light can also be described by using the geometrical parameters of an ellipse, including the amplitude A, the azimuthal angle ψ, and the ellipticity angle φ. The relation between the Stokes parameters and the geometrical ellipse parameters can be described as [18]

$$S_0 = A^2, \tag{9}$$

$$S_1 = A^2 \cos 2\psi \cos 2\varphi, \tag{10}$$

$$S_2 = A^2 \sin 2\psi \cos 2\varphi, \tag{11}$$

$$S_3 = A^2 \sin 2\varphi. \tag{12}$$

Notably, the four independent Stokes parameters can be obtained by measuring the three parameters A, ψ, and φ. Obviously, if we can differentiate the circularly-polarized and linearly-polarized photocurrents induced by the detecting light, the Stokes parameters can be easily obtained. This can be achieved by separately using linear and circular polarization-sensitive photodetectors but requires the fabrication of multiple polarization detectors. In this paper, we find an approach to implement both the linear and circular polarization measurements by using a single 3D TIs thin film device.

In an ideal situation with no linear polarization photoresponse, circular polarization detection can be realized by comparing the measured photocurrent to the calibrated photocurrent to detect the degree of chirality. Specifically, in this case, for a calibrated chirality photodetector, the dependence of the total photocurrent I_{total}, the helicity-dependent photocurrent $I_C = C \sin 2\varphi$, and the polarization-independent current I_D on light power is obtained. Then, the relation between the value I_{total}/I_D and the degree of chirality, i.e., $\sin 2\varphi$, can be abstracted. For the calibrated chirality photodetector, the relation between the I_D and the light power is known. Therefore, the I_D can be determined from the measured photocurrent under a certain light power. By comparing the measured I_{total}/I_D to the calibrated I_{total}/I_D, one can obtain the degree of chirality of the light.

However, the contribution from the additional linear polarization photoresponse prevents it from the accurate quantification of the circular component for light with arbitrary polarization states. To resolve the circular polarization detection using a device with a large linear polarization response, the research about the incident angle dependence of the polarization-dependent photocurrents could be the key. As demonstrated previously, the C, L_1 terms change as an odd function of incident angle, indicating that reversing the incident θ can lead to a huge change of the circular polarization response to the polarization-independent baseline. By comparing the measured photocurrent under opposite incident angles to the calibrated results, the ellipticity angle φ can be determined. Figure 7 shows an example of determining the ellipticity angle φ by this method with the 7-QL $(Bi_{0.8}Sb_{0.2})_2Te_3$/STO sample. In Fig. 7, the solid lines are the dependence of the ratio $I_{\text{total}}/(I_C + I_D)$ of the 7-QL sample under $\theta = \pm 30°$ on the phase angle φ, measured at 77 K under an illumination of 1064 nm laser of 110 mW with $V_{\text{bg}} = -30$ V. These photocurrents are used as the calibrated values, denoted as $I^{\text{cal}}_{\text{total}}/(I^{\text{cal}}_C + I^{\text{cal}}_D)$. Then, by dividing the measured photocurrent, denoted as $I^{\text{mea}}_{\text{total}}$, under $\theta = \pm 30°$ to the calibrated I_C and I_D at different phase angles φ, we obtain the ratio $I^{\text{mea}}_{\text{total}}/(I^{\text{cal}}_C + I^{\text{cal}}_D)$, as illustrated by the dashed lines in Fig. 7. There are four intersections between the solid and short dashed lines. The intersection coordinates at $\varphi = 35°$ are the only common intersection gained under both the positive and negative incident angles, which suggests that the ellipticity angle φ is 35°.

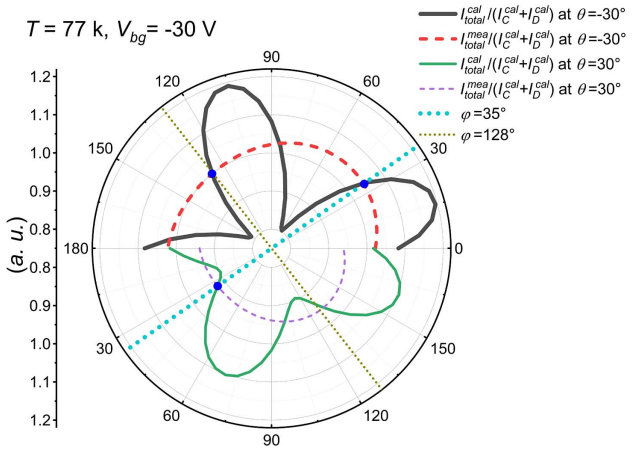

Fig. 7. Dependence of the ratio $I_{\text{total}}/(I_C + I_D)$ of the measured and calibrated photocurrent on the phase angle φ under incident angle $\theta = \pm 30°$. The photocurrent is measured under the light illumination with a power of 110 mW at 77 K and back gate voltage of $V_{\text{bg}} = -30$ V. The intersections of the ratio $I^{\text{mea}}_{\text{total}}/(I^{\text{cal}}_C + I^{\text{cal}}_D)$ and $I^{\text{cal}}_{\text{total}}/(I^{\text{cal}}_C + I^{\text{cal}}_D)$ are marked out at $\varphi = 35°$, 128°.

It is worth mentioning that the reason for applying a back gate voltage of −30 V is that at $V_{\text{bg}} = -30$ V the value of $|C|/(|C| + |L_1| + |L_2|)$ reaches the maximum, as shown in Fig. 3(d), which can improve the accuracy of the circular polarization detection. We set the ratio $I_{\text{total}}/(I_C + I_D)$ as the comparing target because its correlation with CPGE is higher than I_{total} and thus can enhance the detection accuracy.

Figures 8(a) and 8(b) show the dependence of the fitting parameters C, D, L_1, and L_2 on the incident light power for the 7-QL sample. Note that the photocurrent components C, D, L_1, and L_2 show a linear dependence on the light power. Figure 8(c) shows the dependence of the photoconductance on the incident light power in the 7-QL sample, which almost changes linearly with the light power. By measuring a photoconductance under an illumination of a light at $V_{\text{bg}} = -30$ V, the light power can be easily obtained by the calibrated photoconductance. As a result, the Stokes parameter S_0 can be obtained by the photoconductance measurement [49]. Comparing our polarization detection method to the one realized in Bi_2Te_2Se thin films, which separates the circular polarization from the linear polarization by obtaining the differential photocurrent at different bias voltages [49], our method is of wider applicability for 3D TIs thin films. The reason is that their method is easier to implement only when the LPDE is negligible, so that the LPGE current will not be amplified by the bias because of the instantaneous nature of the LPGE. However, besides the LPGE, the LPDE may also show up in 3D TIs [36,41,59], which will make the linear polarization-dependent photocurrent also change with the bias. For example, we observed the considerable LPDE current in our $(Bi_{1-x}Sb_x)_2Te_3$ thin films. As a result, if we apply the bias

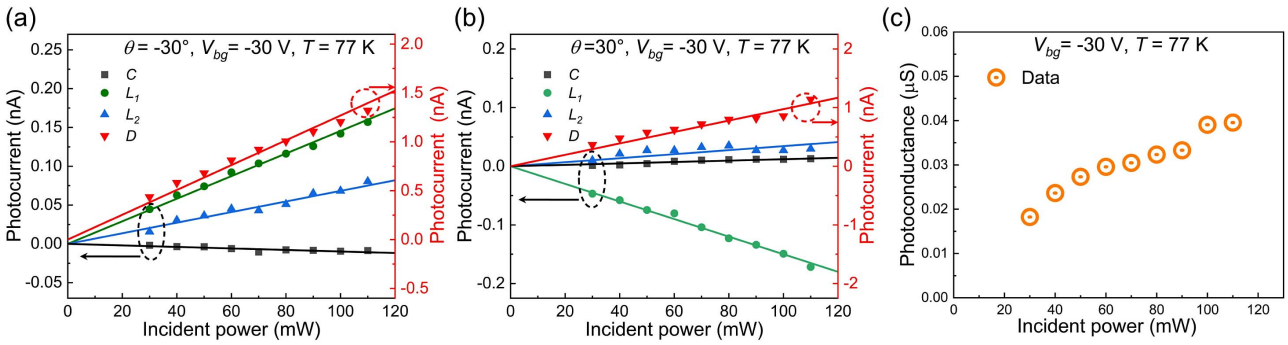

Fig. 8. Dependence of the fitting parameters C, D, L_1, and L_2 on the incident light power in the 7-QL $(Bi_{0.8}Sb_{0.2})_2Te_3$ thin film under an incident angle (a) $\theta = -30°$ and (b) $\theta = 30°$ at 77 K. (c) Dependence of the photoconductance on incident light power in the 7-QL $(Bi_{0.8}Sb_{0.2})_2Te_3$ thin film.

voltages to the $(Bi_{1-x}Sb_x)_2Te_3$ thin films, it will be hard to separate the photoresponse of circular polarization from that of the linear polarization. The polarization detection strategy we proposed can be applied to all kinds of 3D TIs materials. To sum it up, our method for polarization detection is better in applicability for 3D TIs thin films.

For further confirmation, we also use the 10- and 20-QL BST samples to detect the ellipticity angle. We find that the ellipticity angle can also be successfully detected by the 10- and 20-QL samples, but the 7-QL sample shows a better detection accuracy compared to the 10- and 20-QL samples. This is because the ratio of the helicity-dependent photocurrent to the sum of the absolute values of the polarization-dependent photocurrents $|C|/(|C| + |L_1| + |L_2|)$ is larger in the 7-QL sample. Besides, for the 7-QL sample, the detection accuracy is better when applying a back gate voltage of −30 V because the value of $|C|/(|C| + |L_1| + |L_2|)$ reaches the maximum at V_{bg} of −30 V. This phenomenon further confirms that the larger proportion of helicity-dependent photocurrent will improve the detection accuracy of the ellipticity angle.

Based on the method mentioned above, we can obtain the ellipticity angle φ and the light power A^2; hence, we also can obtain the complete polarization states by full-Stokes detection after characterizing the azimuthal angle ψ. To obtain the azimuthal angle ψ, we use the linear polarization detection mode, in which the CPGE (or CPDE) should be almost turned off and the LPGE (or LPDE) currents will play the dominate role. It can be seen from Fig. 3(c) that, to almost turn off the CPGE (or CPDE), one should apply a back gate voltage of 260 V. Under $V_{bg} = 260$ V, the CPGE (or CPDE) is almost turned off. This is because the chemical potential is tuned to the warping region at the conduction band edge where the spin texture is not strictly locked to its momentum, and the electrons are also easily scattered to spin-degenerated states by bulk phonons [51,56].

Figure 9 shows the dependence of the photocurrent, with the polarization-independent current D being subtracted, on the angle of the quarter-wave plate α, which is measured under the same condition as that on the ellipticity angle detection except that the back gate voltage is applied. Considering that $\psi = 2\alpha$, we fit the calibrated photocurrent with the equation $J = 0.15\ \sin(4\alpha + \beta) + 0.06\ \cos(4\alpha)$. Here, the angle β is a fitting parameter, which represents the angle between the a axis of the lattice and the y axis. This is because the LPGE is related to the lattice orientation [57], but the LPDE is not related to the lattice symmetry. Therefore, the $\cos(4\alpha)$ term does not contain any additional angle parameter [36]. By fitting, we obtain $\beta = 0.03\pi$. The measured photocurrent for linear polarization detection is then used to determine the phase angle α within 0° to 90°, by comparing the measured results with the calibrated photocurrent under the opposite light incident angles. For linear polarization detection, it is more reasonable to calculate the ratio $I_{total}/(I_{LPGE} + I_D)$ as the comparing target. Finally, the azimuthal angle $\psi = 2\alpha$ can be substituted into Eqs. (9)–(12) and $\tan(2\psi) = S_2/S_1$ to determine the Stokes parameters $S_{1,2}$. Thus, we demonstrate a way to use the 3D TI BST thin film as an effective miniature single-device for chirality and polarimetry detection.

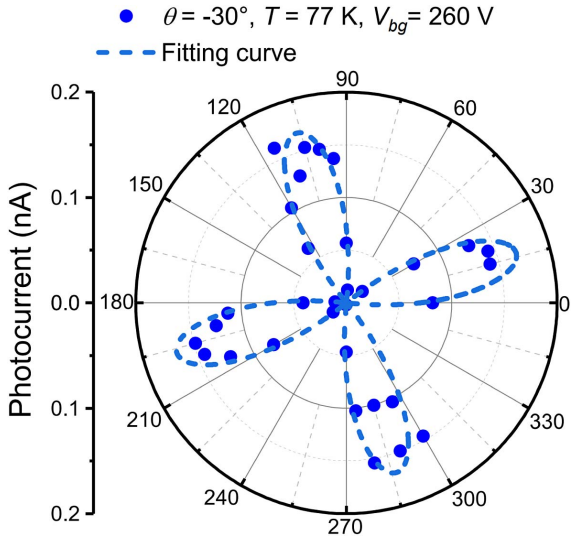

Fig. 9. Dependence of the photocurrent, with the polarization-independent current D being substrated, on the angle of the quarter-wave plate α in the 7-QL BST sample. The photocurrent is measured under a light power of 110 mW and a back gate voltage of 260 V at 77 K.

4. CONCLUSION

In conclusion, we have demonstrated a single device based on 3D TI BST thin films for optical chirality and polarimetry detection. Tuning the back gate voltages can switch the detector to different operating modes for linear or circular polarization detection, respectively. The investigations of the microscopic origin and the gate voltage tuning effect of different components of the polarization-dependent photocurrents in BST thin films provide the theoretical support for polarization detection. Combining the measurements of photocurrents under opposite light incident angles enables chiral photodetectors with a thin film device, and increasing the proportion of the helicity-dependent photocurrent in the total photocurrent by back gating can enhance the detection accuracy. The full Stokes parameters can be extracted by incorporating the measured linear polarization state on the same device. Therefore, the polarization detection method proposed in this work shows potential to be an effective way for chirality and polarimetry detection and can be used in a wide spectrum of applications from biomedical molecules to screening polarimetric imaging.

Funding. National Natural Science Foundation of China (62074036, 61674038, 11574302); Foreign Cooperation Project of Fujian Province (2023I0005); Open Research Fund Program of the State Key Laboratory of Low-Dimensional Quantum Physics (KF202108); National Key Research and Development Program of China (2016YFB0402303); Foundation of Fujian Provincial Department of Industry and Information Technology (82318075).

Disclosures. The authors declare no conflicts of interest.

Data Availability. Data underlying the results presented in this paper are not publicly available at this time but may be obtained from the authors upon reasonable request.

REFERENCES

1. X. Wang, Y. Wang, W. Gao, L. Song, C. Ran, Y. Chen, and W. Huang, "Polarization-sensitive halide perovskites for polarized luminescence and detection: recent advances and perspectives," Adv. Mater. **33**, 2003615 (2021).
2. B. Yang, D. Ma, W. Liu, D.-Y. Choi, Z. Li, H. Cheng, J. Tian, and S. Chen, "Deep-learning-based colorimetric polarization-angle detection with metasurfaces," Optica **9**, 217–220 (2022).
3. J. Bai, C. Wang, X. Chen, A. Basiri, C. Wang, and Y. Yao, "Chip-integrated plasmonic flat optics for mid-infrared full-Stokes polarization detection," Photonics Res. **7**, 1051–1060 (2019).
4. C. Zhang, J. Hu, Y. Dong, A. Zeng, H. Huang, and C. Wang, "High efficiency all-dielectric pixelated metasurface for near-infrared full-Stokes polarization detection," Photonics Res. **9**, 583–589 (2021).
5. W. H. Brooks, W. C. Guida, and K. G. Daniel, "The significance of chirality in drug design and development," Cur. Top. Med. Chem. **11**, 760–770 (2011).
6. C. Wagenknecht, C. M. Li, A. Reingruber, X. H. Bao, A. Goebel, Y. A. Chen, Q. A. Zhang, K. Chen, and J. W. Pan, "Experimental demonstration of a heralded entanglement source," Nat. Photonics **4**, 549–552 (2010).
7. L. F. Li, J. Z. Wang, L. Kang, W. Liu, L. Yu, B. J. Zheng, M. L. Brongersma, D. H. Werner, S. F. Lan, Y. Shi, Y. Xu, and X. M. Wang, "Monolithic full-Stokes near-infrared polarimetry with chiral plasmonic metasurface integrated graphene–silicon photodetector," ACS Nano **14**, 16634–16642 (2020).
8. T. Lepetit and B. Kanté, "Simultaneous Stokes parameters," Nat. Photonics **9**, 709–710 (2015).
9. X. X. Sheng, G. Y. Chen, C. Wang, W. Q. Wang, J. F. Hui, Q. Zhang, K. H . Yu, W. Wei, M. D. Yi, M. Zhang, Y. Deng, P. Wang, X. X. Xu, Z. H. Dai, J. C. Bao, and X. Wang, "Polarized optoelectronics of $CsPbX_3$ (X = Cl, Br, I) perovskite nanoplates with tunable size and thickness," Adv. Funct. Mater. **28**, 1800283 (2018).
10. S. Lim, M. Ha, Y. Lee, and H. Ko, "Large-area, solution-processed, hierarchical MAPbI3 nanoribbon arrays for self-powered flexible photodetectors," Adv. Opt. Mater. **6**, 1800615 (2018).
11. D. Ghoshal, T. M. Wang, H. Z. Tsai, S. W. Chang, M. Crommie, N. Koratkar, and S. F. Shi, "Catalyst-free and morphology-controlled growth of 2D perovskite nanowires for polarized light detection," Adv. Opt. Mater. **7**, 1900039 (2019).
12. Y. Peng, X. T. Liu, Z. H. Sun, C. M. Ji, L. N. Li, Z. Y. Wu, S. S. Wang, Y. P. Yao, M. C. Hong, and J. H. Luo, "Exploiting the bulk photovoltaic effect in a 2D trilayered hybrid ferroelectric for highly sensitive polarized light detection," Angew. Chem. Int. Ed. **59**, 3933–3937 (2020).
13. A. Ishii and T. Miyasaka, "Direct detection of circular polarized light in helical 1D perovskite-based photodiode," Sci. Adv. **6**, eabd3274 (2020).
14. J. Q. Ma, C. Fang, C. Chen, L. Jin, J. Q. Wang, S. Wang, J. Tang, and D. H. Li, "Chiral 2D perovskites with a high degree of circularly polarized photoluminescence," ACS Nano **13**, 3659–3665 (2019).
15. J. Wang, C. Fang, J. Q. Ma, S. Wang, L. Jin, W. C. Li, and D. H. Li, "Aqueous synthesis of low-dimensional lead halide perovskites for room-temperature circularly polarized light emission and detection," ACS Nano **13**, 9473–9481 (2019).
16. A. Papakostas, A. Potts, D. M. Bagnall, S. L. Prosvirnin, H. J. Coles, and N. I. Zheludev, "Optical manifestations of planar chirality," Phys. Rev. Lett. **90**, 107404 (2003).
17. X. Sun, G. Adamo, M. Eginligil, H. N. S. Krishnamoorthy, N. I. Zheludev, and C. Soci, "Topological insulator metamaterial with giant circular photogalvanic effect," Sci. Adv. **7**, eabe5748 (2021).
18. M. Dai, C. Wang, B. Qiang, F. Wang, M. Ye, S. Han, Y. Luo, and Q. J. Wang, "On-chip mid-infrared photothermoelectric detectors for full-Stokes detection," Nat. Commun. **13**, 4560 (2022).
19. A. Basiri, X. H. Chen, J. Bai, P. Amrollahi, J. Carpenter, Z. Holman, C. Wang, and Y. Yao, "Nature-inspired chiral metasurfaces for circular polarization detection and full-Stokes polarimetric measurements," Light Sci. Appl. **8**, 78 (2019).
20. Y. Zhao, A. N. Askarpour, L. Y. Sun, J. W. Shi, X. Q. Li, and A. Alu, "Chirality detection of enantiomers using twisted optical metamaterials," Nat. Commun. **8**, 14180 (2017).
21. Z. Chi, Y.-C. Lau, X. Xu, T. Ohkubo, K. Hono, and M. Hayashi, "The spin Hall effect of Bi-Sb alloys driven by thermally excited Dirac-like electrons," Sci. Adv. **6**, eaay2324 (2020).
22. A. Navabi, Y. Liu, P. Upadhyaya, K. Murata, F. Ebrahimi, G. Yu, B. Ma, Y. Rao, M. Yazdani, M. Montazeri, L. Pan, I. N. Krivorotov, I. Barsukov, Q. Yang, P. Khalili Amiri, Y. Tserkovnyak, and K. L. Wang, "Control of spin-wave damping in YIG using spin currents from topological insulators," Phys. Rev. Appl. **11**, 034046 (2019).
23. H. Wu, P. Zhang, P. Deng, Q. Lan, Q. Pan, S. A. Razavi, X. Che, L. Huang, B. Dai, K. Wong, X. Han, and K. L. Wang, "Room-temperature spin-orbit torque from topological surface states," Phys. Rev. Lett. **123**, 207205 (2019).
24. K. Kondou, R. Yoshimi, A. Tsukazaki, Y. Fukuma, J. Matsuno, K. S. Takahashi, M. Kawasaki, Y. Tokura, and Y. Otani, "Fermi-level-dependent charge-to-spin current conversion by Dirac surface states of topological insulators," Nat. Phys. **12**, 1027–1031 (2016).
25. J. L. Liu, H. Wang, X. Li, H. Chen, Z. K. Zhang, W. W. Pan, G. Q. Luo, C. L. Yuan, Y. L. Ren, and W. Lei, "Ultrasensitive flexible near-infrared photodetectors based on van der Waals Bi_2Te_3 nanoplates," Appl. Surf. Sci. **484**, 542–550 (2019).
26. J. Yu, K. Zhu, X. Zeng, L. Chen, Y. Chen, Y. Liu, C. Yin, S. Cheng, Y. Lai, J. Huang, K. He, and Q. Xue, "Helicity-dependent photocurrent of the top and bottom Dirac surface states of epitaxial thin films of three-dimensional topological insulators Sb_2Te_3," Phys. Rev. B **100**, 235108 (2019).
27. H. Zhang, Z. Song, D. Li, Y. Xu, J. Li, C. Bai, and B. Man, "Near-infrared photodetection based on topological insulator P-N heterojunction of SnTe/Bi_2Se_3," Appl. Surf. Sci. **509**, 145290 (2020).

28. P. Corbae, S. Ciocys, D. Varjas, E. Kennedy, S. Zeltmann, M. Molina-Ruiz, S. M. Griffin, C. Jozwiak, Z. H. Chen, L. W. Wang, A. M. Minor, M. Scott, A. G. Grushin, A. Lanzara, and F. Hellman, "Observation of spin-momentum locked surface states in amorphous Bi_2Se_3," Nat. Mater. **22**, 200–206 (2023).
29. S. Izadi, A. Bhattacharya, S. Salloum, J. W. Han, L. Schnatmann, U. Wolff, N. Perez, G. Bendt, I. Ennen, A. Hutten, K. Nielsch, S. Schulz, M. Mittendorff, and G. Schierning, "Observation of spin-momentum locked surface states in amorphous Bi_2Se_3," Small **19**, 2204850 (2023).
30. G. N. Kozhemyakin, Y. N. Bendryshev, and A. V. Churilov, "Photovoltaic effect in metal foils and crystals of topological insulators," CrystEngComm **25**, 1507–1518 (2023).
31. S. Zhang, C. Shi, W. Tang, L. Zhang, L. Han, C. Yang, Z. Zhang, J. Wang, M. Cai, G. Li, C. Liu, L. Wang, X. Chen, and W. Lu, "High-frequency enhanced response based on Sb_2Te_3 topological insulators," Photonics Res. **10**, 2302–2308 (2022).
32. M. Z. Hasan and C. L. Kane, "Colloquium: topological insulators," Rev. Mod. Phys. **82**, 3045–3067 (2010).
33. J. E. Moore, "The birth of topological insulators," Nature **464**, 194–198 (2010).
34. X. L. Qi and S. C. Zhang, "Topological insulators and superconductors," Rev. Mod. Phys. **83**, 1057–1110 (2011).
35. J. H. Bardarson and J. E. Moore, "Quantum interference and Aharonov–Bohm oscillations in topological insulators," Rep. Prog. Phys. **76**, 056501 (2013).
36. H. Plank, L. E. Golub, S. Bauer, V. V. Bel'kov, T. Herrmann, P. Olbrich, M. Eschbach, L. Plucinski, C. M. Schneider, J. Kampmeier, M. Lanius, G. Mussler, D. Grützmacher, and S. D. Ganichev, "Photon drag effect in $(Bi_{1-x}Sb_x)_2Te_3$ three-dimensional topological insulators," Phys. Rev. B **93**, 125434 (2016).
37. J. D. Yao, J. M. Shao, S. W. Li, D. H. Bao, and G. W. Yang, "Polarization dependent photocurrent in the Bi_2Te_3 topological insulator film for multifunctional photodetection," Sci. Rep. **5**, 14184 (2015).
38. A. M. Shikin, I. I. Klimovskikh, M. V. Filyanina, A. A. Rybkina, D. A. Pudikov, K. A. Kokh, and O. E. Tereshchenko, "Surface spin-polarized currents generated in topological insulators by circularly polarized synchrotron radiation and their photoelectron spectroscopy indication," Phys. Solid State **58**, 1675–1686 (2016).
39. D. A. Bas, K. Vargas-Velez, S. Babakiray, T. A. Johnson, P. Borisov, T. D. Stanescu, D. Lederman, and A. D. Bristow, "Coherent control of injection currents in high-quality films of Bi_2Se_3," Appl. Phys. Lett. **106**, 041109 (2015).
40. J. Sánchez-Barriga, E. Golias, A. Varykhalov, J. Braun, L. V. Yashina, R. Schumann, J. Minár, H. Ebert, O. Kornilov, and O. Rader, "Ultrafast spin-polarization control of Dirac fermions in topological insulators," Phys. Rev. B **93**, 155426 (2016).
41. Y. Pan, Q. Z. Wang, A. L. Yeats, T. Pillsbury, T. C. Flanagan, A. Richardella, H. Zhang, D. D. Awschalom, C. X. Liu, and N. Samarth, "Helicity dependent photocurrent in electrically gated $(Bi_{1-x}Sb_x)_2Te_3$ thin films," Nat. Commun. **8**, 1037 (2017).
42. J. W. McIver, D. Hsieh, H. Steinberg, P. Jarillo-Herrero, and N. Gedik, "Control over topological insulator photocurrents with light polarization," Nat. Nanotechnol. **7**, 96–100 (2011).
43. P. Hosur, "Circular photogalvanic effect on topological insulator surfaces: Berry-curvature-dependent response," Phys. Rev. B **83**, 035309 (2011).
44. V. A. Shalygin, H. Diehl, C. Hoffmann, S. N. Danilov, T. Herrle, S. A. Tarasenko, D. Schuh, C. Gerl, W. Wegscheider, W. Prettl, and S. D. Ganichev, "Spin photocurrents and the circular photon drag effect in (110)-grown quantum well structures," JETP Lett. **84**, 570–576 (2007).
45. W. Weber, L. E. Golub, S. N. Danilov, J. Karch, C. Reitmaier, B. Wittmann, V. V. Bel'kov, E. L. Ivchenko, Z. D. Kvon, N. Q. Vinh, A. F. G. van der Meer, B. Murdin, and S. D. Ganichev, "Quantum ratchet effects induced by terahertz radiation in GaN-based two-dimensional structures," Phys. Rev. B **77**, 245304 (2008).
46. C. Kastl, C. Karnetzky, H. Karl, and A. W. Holleitner, "Ultrafast helicity control of surface currents in topological insulators with near-unity fidelity," Nat. Commun. **6**, 6617 (2015).
47. K. N. Okada, N. Ogawa, R. Yoshimi, A. Tsukazaki, K. S. Takahashi, M. Kawasaki, and Y. Tokura, "Enhanced photogalvanic current in topological insulators via Fermi energy tuning," Phys. Rev. B **93**, 081403 (2016).
48. Y. M. Wang, J. L. Yu, X. L. Zeng, Y. H. Chen, Y. Liu, S. Y. Cheng, Y. F. Lai, C. M. Yin, K. He, and Q. K. Xue, "Temperature and excitation wavelength dependence of circular and linear photogalvanic effect in a three dimensional topological insulator Bi_2Se_3," J. Phys. Condens. Matter **31**, 415702 (2019).
49. S. Huang and X. Xu, "Optical chirality detection using a topological insulator transistor," Adv. Opt. Mater. **9**, 2002210 (2021).
50. S. D. Ganichev and W. Prettl, "Spin photocurrents in quantum wells," J. Phys. Condens. Matter **15**, R935–R983 (2003).
51. S. Huang, I. Miotkowski, Y. P. Chen, and X. Xu, "Deep tuning of photothermoelectricity in topological surface states," Sci. Rep. **10**, 16761 (2020).
52. C. Jiang, V. A. Shalygin, V. Y. Panevin, S. N. Danilov, M. M. Glazov, R. Yakimova, S. Lara-Avila, S. Kubatkin, and S. D. Ganichev, "Helicity-dependent photocurrents in graphene layers excited by midinfrared radiation of a CO_2 laser," Phys. Rev. B **84**, 125429 (2011).
53. X. L. Zeng, J. L. Yu, S. Y. Cheng, Y. F. Lai, Y. H. Chen, and W. Huang, "Temperature dependence of photogalvanic effect in GaAs/AlGaAs two-dimensional electron gas at interband and intersubband excitation," J. Appl. Phys. **121**, 193901 (2017).
54. F. Yang, A. A. Taskin, S. Sasaki, K. Segawa, Y. Ohno, K. Matsumoto, and A. Yoichi, "Dual-gated topological insulator thin-film device for efficient Fermi-level tuning," ACS Nano **9**, 4050–4055 (2021).
55. Y. H. Wang, D. Hsieh, D. Pilon, L. Fu, D. R. Gardner, Y. S. Lee, and N. Gedik, "Observation of a warped helical spin texture in Bi_2Se_3 from circular dichroism angle-resolved photoemission spectroscopy," Phys. Rev. Lett. **107**, 207602 (2011).
56. M. S. Bahramy, P. D. C. King, A. de la Torre, J. Chang, M. Shi, L. Patthey, G. Balakrishnan, P. Hofmann, R. Arita, N. Nagaosa, and F. Baumberger "Emergent quantum confinement at topological insulator surfaces," Nat. Commun. **3**, 1159 (2012).
57. H. Plank, S. N. Danilov, V. V. Bel'kov, V. A. Shalygin, J. Kampmeier, M. Lanius, G. Mussler, D. Grützmacher, and S. D. Ganichev, "Optoelectronic characterization of three dimensional topological insulators," J. Appl. Phys. **120**, 165301 (2016).
58. C. Yin, H. Yuan, X. Wang, S. Liu, S. Zhang, N. Tang, F. Xu, Z. Chen, H. Shimotani, Y. Iwasa, Y. Chen, W. Ge, and B. Shen, "Tunable surface electron spin splitting with electric double-layer transistors based on InN," Nano Lett. **13**, 2024–2029 (2013).
59. L. Braun, G. Mussler, A. Hruban, M. Konczykowski, T. Schumann, M. Wolf, M. Münzenberg, L. Perfetti, and T. Kampfrath, "Ultrafast photocurrents at the surface of the three-dimensional topological insulator Bi_2Se_3," Nat. Commun. **7**, 13259 (2016).